Materials Today Communications 32 (2022) 103835

Contents lists available at ScienceDirect

Materials Today Communications

journal homepage: www.elsevier.com/locate/mtcomm

One-step fluorine-free synthesis of delaminated, OH-terminated Ti_3C_2: High photocatalytic NO_x storage selectivity enabled by coupling TiO_2 and Ti_3C_2-OH

Ahmed Al Mayyahi [a], Swagotom Sarker [a], Brian M. Everhart [a], Xiaoqing He [b], Placidus B. Amama [a,*]

[a] Tim Taylor Department of Chemical Engineering, Kansas State University, Manhattan, KS 66506, United States
[b] Electron Microscopy Core and Department of Mechanical & Aerospace Engineering, University of Missouri, Columbia, MO 65211, United States

ARTICLE INFO

Keywords:
MXene (Ti_3C_2-OH)
One-step synthesis
TiO_2
TiO_2-Ti_3C_2-OH hybrid
Photocatalysis
NO_x oxidation

ABSTRACT

Difficulties associated with MXene fabrication typified by an environmentally hazardous fluorine-based etching process followed by delamination and fluorine reduction steps create obstacles against the expansion of this outstanding material and its application in air purification. Herein, we demonstrate a one-step hydrothermal process that involves alkali (NaOH)-assisted aluminum etching in the presence of a delaminating agent (hydrazine) for synthesis of delaminated, OH-terminated MXene (Ti_3C_2-OH). The process does not require the use of fluorine-containing compounds and produces Ti_3C_2-OH sheets without the need for post-synthesis treatment. Ti_3C_2-OH shows a strong synergistic effect as a co-catalyst when coupled with TiO_2 during photocatalytic oxidation of NO_x. Excellent NO_x storage selectivity (91 %) and a positive $DeNO_x$ index (+ 0.30) were achieved at NO conversion of 54 %. The photocatalytic activity of the hybrid shows high sensitivity to the surface chemistry of the co-catalyst as Ti_3C_2-OH outperforms delaminated, F-terminated Ti_3C_2 (fabricated via the traditional process), which shows low NO_x storage selectivity (65 %) and a negative $DeNO_x$ index (−0.05) at NO conversion of 47 %. We envision that these findings will benefit ongoing efforts aimed at developing effective alternative methods for MXene synthesis and provide a pathway for rational design of efficient NO_x abatement photocatalysts.

1. Introduction

MXenes, first fabricated at Drexel University by selective elimination of an A (typically group IIIA or IVA of the periodic table) element from MAX phase, are 2D layered ternary materials with the general formula of $M_{n+1}X_n$ (M = transition metal; X = carbon or nitrogen; and $n = 1, 2,$ or 3) [1,2]. Elimination of the A element in MAX phase results in a multi-layered structure that is terminated by functional groups (such as =O, -OH and/or -F) and stabilized via van der Waals or hydrogen bonding interactions, which is then delaminated into thin flakes by chemical intercalation with large-size organic molecules [3]. Generally, single- or few-layer MXene sheets offer an appealing combination of high ionic mobility, electrical conductivity, and chemical stability, as well as tunable structure and surface chemistry that are desired in many important applications [4,5]. Even though the two-step etching-delamination process produces single- or few-layer 2D-MXene sheets, it requires high production cost and is environmentally harmful when fluorine-containing compounds are involved [1–3]. Therefore, a one-step etching-delamination approach that is free of fluorine is needed.

Recent studies have highlighted the impact of functional groups attached to the planar Ti_3C_2 surfaces on their physical properties and performance in environmental applications. For instance, the adsorption of NO_2 is favored on Ti_3C_2, particularly on OH-terminated Ti_3C_2 in the form of nitrites — a phenomenon that has been utilized to design effective NO_2 sensors [6–8]. Also, theoretical studies [9,10] revealed the Fermi level of Ti_3C_2 strongly relies on its surface terminal groups. In particular, OH-terminated Ti_3C_2 has been shown to have an ultralow work function (1.6–2.8 eV), which can serve as a hole reservoir when coupled with TiO_2 facilitating electron-hole separation and subsequent photocatalytic activity [11–13]. Therefore, the surface chemistry of Ti_3C_2 can be tuned to suit the desired application. Nevertheless,

* Corresponding author.
E-mail address: pamama@ksu.edu (P.B. Amama).

https://doi.org/10.1016/j.mtcomm.2022.103835
Received 26 February 2022; Received in revised form 27 May 2022; Accepted 10 June 2022
Available online 18 June 2022
2352-4928/© 2022 Elsevier Ltd. All rights reserved.

utilization of Ti_3C_2 in photocatalytic air purification has been limited due to the lack of a rational framework for harnessing its properties in the design of photocatalysts.

Photocatalysis is an attractive approach for practical oxidation of NO_x (one of the criteria air pollutants according to the U.S. Environmental Protection Agency (EPA)) due to its strong ability to oxidize NO_x under ambient conditions and at relatively low concentrations. Photocatalytic NO_x oxidation can potentially serve as an alternative to traditional NO_x abatement approaches especially for NO_x pollution at part-per-billion (ppb) levels and in the presence of other pollutants (e.g., VOCs, SO_x, etc.) [14]. In addition, a hybrid approach that combines photocatalysis and a traditional approach (adsorption, plasma, or reduction) could lead to efficient removal of high levels of NO_x from industrial waste streams (flue gas). Although TiO_2 (P25, Degussa) is the gold standard photocatalyst under UV light, it possesses low selectivity towards NO_x storage in solid state and tends to convert NO to NO_2, a considerably more toxic form of NO_x, especially in humid environment [15]. In other words, TiO_2 oxidizes NO to NO_2 but fails to store the produced NO_2 on catalyst surface in the forms of other non-volatile and less toxic compounds such as HNO_3, NO_3^- or NO_2^-. The low NO_x storage selectivity has limited the practical application of TiO_2 in NO_x abatement. To improve the activity of TiO_2 in NO_x oxidation, two broad strategies classified as photocatalytic and non-photocatalytic have been explored. Photocatalytic processes involve enhancing electron-hole separation through coupling TiO_2 with nanocarbon (i.e. graphene) or creating defects in TiO_2 lattice to facilitate the generation of reactive oxygen species (ROS) and storage of NO_2 on catalyst surface in the form of HNO_3 [16,17]. Non-photocatalytic processes involve coupling TiO_2 with non-photocatalytic nanostructures that can provide NO_x storage (adsorption) sites to store NO_2 on the catalyst surface in the form of NO_3^- or NO_2^- [18,19]. Thus, due to its high affinity towards NO_2 adsorption and its ultralow work function, OH-terminated Ti_3C_2 appears to be well suited for coupling with TiO_2 to reduce charge carrier recombination and provide non-photocatalytic adsorption sites for NO_x storage, and thereby, effectively removing NO_x.

Herein, delaminated, OH-terminated Ti_3C_2 (designated as Ti_3C_2-OH) sheets were fabricated in a single step and successfully coupled with commercial TiO_2 (P25, Degussa) to form hybrid photocatalysts. Fabrication of Ti_3C_2-OH was achieved using NaOH (etchant) and hydrazine (delaminating agent) to simultaneously extract Al from Ti_3AlC_2 and delaminate the sheets. Unique features of the one-step process are that it utilizes hydrazine-derived intercalants as alternatives to traditional liquid intercalants in a separate step, and it does not require the use of fluorine-containing etchants. Coupling TiO_2 and Ti_3C_2-OH results in a strong synergistic effect that promotes photocatalytic abatement of NO_x.

2. Experimental

2.1. One-step etching and delamination of Ti_3AlC_2

One mmole Ti_3AlC_2 (Carbon, Ukraine; particle size: 40 μm) was dispersed in 120 mL distilled water and 15 mL 70 % hydrazine (Sigma-Aldrich, USA) was slowly added to it. Then, 0.12 mol NaOH (Sigma-Aldrich, USA) as the etching agent was also dissolved in the above solution. The solution was transferred to a 200 mL Teflon-lined hydrothermal autoclave and placed in an electric oven at 180 °C for 24 h. After cooling the reactor to room temperature, the sample was collected by vacuum filtration aided by water and methanol. The collected sample was dried at room temperature and designated as E-Ti_3AlC_2.

2.2. Two-step etching and delamination of Ti_3AlC_2

One mmole Ti_3AlC_2 of size of $\leq$ 40 μm was dispersed in 135 mL distilled water. Then, 0.12 mol NaOH as the etching agent was also dissolved in the above solution. The solution was transferred to a 200 mL Teflon-lined hydrothermal autoclave and placed in an electric oven at 180 °C for 24 h. After cooling the reactor to room temperature, sample was collected by vacuum filtration aided by water and methanol. A section (130 mg) of produced structure was delaminated in 10 mL hydrazine under stirring at room temperature for 24 h. The final product was collected by vacuum filtration aided by water and methanol. The collected sample was dried at room temperature and designated as E-Ti_3AlC_2-2.

2.3. Etching of Ti_3AlC_2 using LiF/HCl solution

LiF (1 g, Sigma-Aldrich, USA) was added to 10 mL 9 M HCl (Sigma-Aldrich, USA) and a magnetic stirrer was placed inside. 1 g Ti_3AlC_2 was mixed with the solution slowly. After adding Ti_3AlC_2 powder, the solution was maintained at 40 °C for 36 h and stirred at 300 rpm. A Teflon lid was gently placed on the Teflon container. The final product was collected by vacuum filtration aided by water and methanol. The collected sample was dried at room temperature and designated as LiF-Ti_3AlC_2.

2.4. Synthesis of TiO_2-Ti_3C_2-OH and TiO_2-Ti_3C_2-F photocatalysts

E-Ti_3AlC_2 (137 mg) was dispersed in 30 mL distilled water by sonication for 60 min. The dispersion was split into two parts and centrifuged at 4000 rpm for 15 min. The supernatant containing Ti_3C_2-OH was dropped slowly into the TiO_2 dispersion (2 g P25 in 100 mL distilled water) under stirring for 4 h. Thereafter, TiO_2-Ti_3C_2-OH was collected by centrifugation and dried in air. For TiO_2 coupled with F-terminated Ti_3C_2, the above procedure was followed, except that LiF-Ti_3AlC_2 was used; the resulting hybrid photocatalyst is designated as TiO_2-Ti_3C_2-F.

2.5. Synthesis of other TiO_2-based photocatalysts

Anatase TiO_2 (100 nm) was purchased from US Research Nanotechnology, Inc and used without modification. TiO_2 nucleation on OH-terminated Ti_3C_2 and F-terminated Ti_3C_2 was achieved by thermal treatment following the process reported by Li et al. [20] and designated as Ti_3C_2-OH-400 and Ti_3C_2-F-400, respectively. Briefly, 300 mg of LiF-Ti_3AlC_2 or alkali-treated LiF-Ti_3AlC_2 was placed in a tube furnace and calcined in air at 400 °C for 4 h. The final products were stored in air until next use. For TiO_2-graphene hybrid, graphene synthesised by a catalyst-free gas phase hydrocarbon detonation process [21] using O_2 and C_2H_2 as precursors was received from Sorensen's group. The as-received graphene (137 mg) was dispersed in 30 mL distilled water by sonication for 1 h. Then, the dispersion was slowly dropped into TiO_2 dispersion (2 g P25 in 100 mL distilled water) under stirring and kept under stirring for 4 h. Thereafter, TiO_2-graphene was collected by centrifugation and dried in air. TiO_2 impregnated with Ni was fabricated by a photo-deposition approach using a mixture of $NiCl_2$ and ethanol. Two different solutions were first prepared. Solution A was composed of 2 mg of $NiCl_2$ dispersed in 20 mL distilled water while solution B was composed of 2 g of TiO_2 (P25) dispersed in 5 mL ethanol. Solution B was slowly dropped into solution A under stirring and the pH of the mixture was adjusted to 8 using 0.1 M NaOH aqueous solution. The mixture was irradiated with UV light for 3 h. The final product (designated as TiO_2-Ni) was collected by centrifugation and dried in air.

2.6. Photocatalyst performance evaluation

2.6.1. Substrate preparation

The prepared photocatalyst was sieved to $<$ 125 μm and dispersed in ethanol at a ratio of 0.15 g/mL via sonication for 15 min. The dispersion was poured onto a glass slide (50 $\times$ 100 mm) and cast with a doctor blade to 250 μm. The slide was then allowed to dry before it was used in the photocatalytic reaction.

2.6.2. Reactor configuration

The photocatalytic experiment was conducted at room temperature in a continuous-flow reactor built in accordance with ISO standards except that a lower headspace distance (3 mm) was used due to the insightful results of our previous study where a detailed description of the reactor is provided [15]. The reactor was connected to two gas cylinders containing 100 ppm NO in N_2 and breathing air as shown in Fig. S1. Mass flow controllers were used to monitor the flow rate of gases to the reactor. A SensorPush HT1 humidity sensor was utilized to control the humidity on the inlet gas mixture. The reaction chamber was constructed from steel with a quartz glass window allowing UV light penetration to the photocatalyst surface; the light intensity and wavelength were 2 mW/cm and 320 nm, respectively. NO and NO_x concentrations were measured by Chemiluminescent 42 C Low Source analyzer (Thermo Fisher Scientific).

2.6.3. Activity measurement

A substrate coated with a photocatalyst was loaded into the reactor and irradiated with UV light for one hour under continuous airflow to remove adsorbed contaminants. Then, the light was turned off and NO_x was introduced to the reactor for adequate adsorption of gaseous molecules on the photocatalyst surface. After 30 min, the light was turned on and the reaction was continued at 1.0 ppm NO_x and a total airflow of 3000 sccm with relative humidity of 50 %. After 2 h of reaction, the light was turned off and NO_x was allowed to re-equilibrate. Average concentrations of NO, NO_2 and NO_x were determined by averaging all data obtained during the oxidation reaction.

To further examine the photocatalytic activity, $DeNO_x$ index, an objective figure of merit for photocatalytic NO_x abatement, was utilized. The $DeNO_x$ index is a measure of photonic efficiency during NO_x photocatalytic oxidation; it was proposed as a parameter to quantify the net NO_x removal by considering NO conversion as well as product selectivity, defined as the percentage of NO completely oxidized to nitrates versus the total amount of NO oxidized to NO_2. To calculate DeNOx index, the photonic efficiency for NO, NO_2 and NO_x was first calculated using Eq. (1) [22].

$$\xi = \frac{(c_d - c_i)\dot{V}p}{\varphi ART} \tag{1}$$

where ξ is the photonic efficiency of a given specie; c_d is the species concentrations in the dark; c_i is the species concentrations under illumination; $\dot{V}$ is the volumetric flow rate; p is the pressure in the system (1 atm); φ is the photon flux at the photocatalyst surface (dependent on light wavelength and intensity); A is the catalyst irradiated area; R is the gas constant; and T is the temperature. The calculated photonic efficiencies were then used to calculate the $DeNO_x$ index and the selectivity using Eqs. (2) and (3), respectively.

$$DeNO_x = \xi_{NO_x}\left(3 - \frac{2}{S}\right) \tag{2}$$

$$S = \frac{\xi_{NO_x}}{\xi_{NO}} \tag{3}$$

3. Results and discussion

To extract Al from Ti_3AlC_2 by alkali treatment, an elevated temperature is needed [23,24]. Therefore, Ti_3AlC_2 was immersed in a hydrothermal reactor containing aqueous solution of NaOH and hydrazine, and the reaction was conducted at 180 °C for 24 h. At this temperature, phase transition of hydrazine from liquid to gas occurs, and generates gaseous molecules (N_2, H_2, and NH_3 [25]); it is probable that NH_3 forms an equilibrium between gas and liquid states under the reaction conditions facilitating simultaneous etching and delamination. In this one-step process, the surface Al atoms gradually oxidize and the compounds formed *dissociate* in water by OH attack to form $Al(OH)_4^-$ while the generated NH_4^+ ions replace Al atoms and prevent Ti-layer stabilization, producing Ti_3C_2-OH that can be collected by centrifugation, as depicted in Fig. 1.

The morphology of Ti_3AlC_2 and E-Ti_3AlC_2 was characterized by scanning electron microscopy (SEM) equipped with energy dispersive X-ray spectroscopy (EDS) and transmission electron microscopy (TEM). The SEM image of Ti_3AlC_2 (Fig. 2a) shows the typical layered structure of MAX phase, where the layers are connected. After the hydrothermal treatment and Al etching, the connected layers were separated and thin Ti_3C_2-OH sheets were generated. The SEM images of E-Ti_3AlC_2 (Figs. 2b and S2) show the generation of Ti_3C_2-OH sheets on the surface of Ti_3AlC_2 which were then collected by sonication and centrifugation and subsequently drop cast on a Gilder imaging grid. The SEM image of collected Ti_3C_2-OH showed that the sheets are thin and have lateral size of approximately one micrometer (Fig. 2c). A TEM image of collected Ti_3C_2-OH (Fig. 2d) confirms the generation of thin and transparent sheets that are either single or few sheets (indicated by yellow arrows); this observation is further supported by a high-magnification TEM image (Fig. 2e) and a zoomed-in TEM image (Fig. 2f) that show a two-layer thick Ti_3C_2-OH sheet with a monolayer thickness of ~ 1 nm. Our TEM analysis also reveals the presence of one-layer thick Ti_3C_2-OH sheets (Fig. S3a and b). Elemental composition data from EDS reveal that Ti, C and O were homogeneously distributed over the delaminated Ti_3C_2-OH sheets with low Al content (Fig. 2h), indicating the successful removal of a large fraction of Al.

X-ray diffraction (XRD) patterns of Ti_3AlC_2 and E-Ti_3AlC_2 are presented in Fig. 3a. Both Ti_3AlC_2 and E-Ti_3AlC_2 show almost similar XRD patterns, and the characteristic diffraction peaks corresponding to crystal planes inherited from the Ti_3AlC_2 are obvious in E-Ti_3AlC_2, consistent with other studies in which alkali was used as etchant to remove Al atoms [24,26]. The slight reduction in the intensity of the peak corresponding to (002) plane (clearly shown in the zoomed-in XRD patterns, Fig. S4) and the disappearance of peaks indicated by green arrows in Fig. 3a suggest the destruction of the ordered crystal structure of Ti_3AlC_2 after the etching process is due to the removal of surface Al atoms [26]. The Raman spectra of Ti_3AlC_2 and E-Ti_3AlC_2 are shown in Fig. 3b. The characteristic peaks at 116, 145 and 260 cm^{-1} (labeled as 1, 2 and 3, respectively), attributed to the vibration of Ti and Al in Ti_3AlC_2, vanished after the one-step process due to structure deterioration as a result of Al removal [27–29]. The peaks at 399 and 610 cm^{-1} (labeled 4 and 5, respectively), attributed to the vibration of C and Ti in Ti_3C_2, are broadened after the one-step process due to functional group attachment [29,30]; the broad Raman peaks at 399 and 610 cm^{-1} are attributed to OH-terminated Ti_3C_2 [30]. The G- and D-bands of carbon at 1350 and 1580 cm^{-1} for E-Ti_3AlC_2 in Fig. S5 are broadened, which indicates the presence of free carbons in the sample and corroborates the removal of Al [31,32].

The XPS survey scan of E-Ti_3AlC_2 reveals the presence of C, Ti and O (Fig. 3c); unlike Ti_3AlC_2, no peak corresponding to Al is detected with noticeable increase in O signal. The high-resolution XPS scan in Al 2p region of E-Ti_3AlC_2 (Fig. 3d) reveals considerable reduction in the intensity of peaks corresponding to Al-Ti (71.5 eV) and Al-O (74 eV) [23]. The peak corresponding to C-Ti in C 1s region of E-Ti_3AlC_2 (Fig. 3e) shifted to a slightly higher binding energy when compared to that of Ti_3AlC_2, which is consistent with a previous study [33] and attributed to the attachment of functional groups to the Ti_3C_2 surface. In addition, the peak at 454 eV in Ti 2p region (Fig. 3f) corresponding to Ti-Al bond dramatically decreases in intensity for E-Ti_3AlC_2 while the intensity of peaks corresponding to Ti-O at 458 eV (Ti $2p_{3/2}$) and 464 eV (Ti $2p_{3/2}$) increases [20,23]. Peak fitting of high-resolution scans in Ti 2p of E-Ti_3AlC_2 required multiple components; peak components at 454.4 and 455.8 eV are attributed to Ti-C and C-Ti-OH bonds, respectively (Fig. S6c and d) [34,35]. This indicates Al removal and formation of Ti_3C_2-OH and TiO_2 after the one-step process. Peak fitting of high-resolution scans

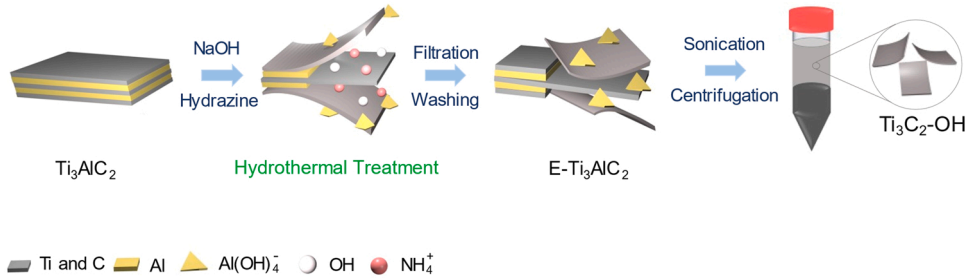

Fig. 1. Schematic illustration of the one-step synthesis of Ti_3C_2-OH involving hydrazine decomposition during alkali treatment.

in O 1s region of E-Ti_3AlC_2 also confirms the generation of Ti_3C_2-OH after the one-step process (Fig. S6). Furthermore, XPS quantitative elemental analysis data (Table S1) show the Al and O atomic percentages decrease and increase in Ti_3AlC_2 and E-Ti_3AlC_2, respectively, as a result of Al extraction, functional group attachment, and formation of TiO_2. XRD, Raman and XPS data confirm the successful removal of Al atoms and subsequent generation of Ti_3C_2-OH during the simultaneous etching and delamination process. It is important to mention that the formation of TiO_2 is only detected by XPS as peaks associated with TiO_2 are absent in the Raman spectra, indicating that the etched portion of the sample consisted mainly of T_3C_2-OH and the formation of TiO_2 is limited to the surface. The mild oxidation of MXene may have occurred during the etching process or post-etching steps (washing, storage, characterization, etc.) as observed in other MXene synthesis studies involving hydrothermal alkali-assisted etching [26,36].

To compare the efficiency of the one-step process to the two-step, we treated Ti_3AlC_2 with NaOH at 180 °C and then used hydrazine as a delaminating agent in a second step at room temperature. The resulting sample is denoted as E-Ti_3AlC_2-2, from which the delaminated Ti_3C_2-OH was collected by sonication and centrifugation steps similar to those used for one-step synthesis of Ti_3C_2-OH (Fig. 1). XPS and EDS analysis of E-Ti_3AlC_2-2 also confirmed Al removal by the two-step process (Figs. S7 and S8). Based on initial evidence from the SEM images (Fig. S9), superior delamination was achieved with the one-step process. In addition, unlike TEM images in Fig. 2 that show the generation of thin sheets for Ti_3C_2-OH from the one-step process, TEM images (Fig. S10) of Ti_3C_2-OH from the two-step process clearly reveal the generation of thick sheets.

The low-quality sheets from delamination using the two-step process is attributed to the interlayer interaction between MXene sheets and subsequent formation of chemical bonds between them. It has been suggested that after Al removal, MXene sheets are stabilized by the formation of bonds with high bonding energy, specifically Ti-Ti and Ti-Al bonds involving residual Al atoms, in addition to hydrogen or van der Waals bonds [37]. In the traditional post-etching process, typically conducted at room temperature, the delaminating agent cannot easily surmount the high energy barrier and intercalate between MXene layers. This means that in the absence of an additional driving force, such as elevated temperature, the rate of intercalation is relatively slow. In contrast, an instantaneous exchange can occur between Al atoms and the delaminating agent during Al etching in the one-step process in the presence of hydrazine at elevated temperature. The interactions between the sheets and subsequent formation of Ti-Ti and Ti-Al bonds are hindered, resulting in the formation of delaminated MXene sheets in one step. Our results indicate the one-step process leads to better delamination in comparison to the two-step process, without compromising the efficiency of Al removal. It is meaningful to point out that the addition of an antioxidant to MXene solution is an effective route to mitigate its oxidation during hydrothermal treatment [37]. Because hydrazine is an antioxidant, its presence in the reaction medium is expected to diminish the oxidation of MXene, especially at elevated temperature (i.e. 270 °C) where severe MXene oxidation occurs [23].

Delaminated, Ti_3C_2-OH was obtained from E-Ti_3AlC_2 via sonication and centrifugation as described earlier and coupled with commercial TiO_2 via a facile hydration and dehydration approach to produce a hybrid photocatalyst (TiO_2-Ti_3C_2-OH). Based on the XRD data, no peaks corresponding to Ti_3C_2-OH were detected in TiO_2-Ti_3C_2-OH due to its low content in the hybrid structure (Fig. S11), consistent with other studies [38,39]. The diffraction peaks were indexed to several crystal planes of anatase TiO_2 (JCPDS No. 21–1272) and facets of rutile TiO_2 (JCPDS No. 21–1276) [39]. The TEM image of TiO_2-Ti_3C_2-OH (Fig. S12a) indicates the TiO_2 particles are supported on Ti_3C_2-OH. The high-resolution TEM image (Fig. S12b) shows the intimate interfacial contact between TiO_2 and Ti_3C_2-OH, which is crucial for improved charge carrier mobility in TiO_2-Ti_3C_2-OH [40]. As expected, no peak corresponding to Al in TiO_2-Ti_3C_2-OH was detected by XPS as shown in the survey scan (Fig. S13a) . The high-resolution XPS spectra in Ti 2p region of TiO_2 and TiO_2-Ti_3C_2-OH demonstrate the Ti 2p doublets of Ti^{4+} ions (Fig. S14a). The O 1s XPS spectra (Fig. S14b) revealed the presence of lattice oxygen (529.3 eV) and –OH surface group (531.2 eV). Since Ti and O coexist in TiO_2 and Ti_3C_2-OH, the characteristic peaks of Ti and O in TiO_2-Ti_3C_2-OH are expected to overlap. Because the amount of Ti_3C_2-OH is significantly lower than that of TiO_2 in TiO_2-Ti_3C_2-OH, the dominant peaks associated with Ti and O in the XPS analysis of TiO_2-Ti_3C_2-OH are mainly attributed to TiO_2. Note that a small amount of C is typically detected in TiO_2 due to the presence of oxygen-containing carbonaceous contaminants (Fig. S13b) [41]. Therefore, C bonds have not been analyzed because it is unclear whether the detected C is from the TiO_2 or Ti_3C_2-OH.

Interestingly, the binding energies of Ti 2p and O 1s in TiO_2-Ti_3C_2-OH showed noticeable shift to lower values compared to those of TiO_2. The shift is attributed to electron transfer from Ti_3C_2-OH with a low work function to TiO_2 with a high work function, further confirming the intimate interaction between the two components and formation of a metal-semiconductor heterojunction [42,43]. Xu et al. [43] observed similar shifts in the binding energies of Ti and O when a heterojunction between TiO_2 (high work function component) and $CsPbBr_3$ (low work function component) was formed via self-assembly coupling. The heterojunction formed in TiO_2-Ti_3C_2-OH is expected to improve electron-hole separation by allowing the transfer of holes from TiO_2 to Ti_3C_2-OH, resulting in improved NO_x photocatalytic oxidation.

The photocatalytic activity of TiO_2-Ti_3C_2-OH was evaluated and compared to pristine TiO_2 and a hybrid photocatalyst (TiO_2-Ti_3C_2-F) fabricated by coupling TiO_2 with delaminated, F-terminated Ti_3C_2 (most widely used MXene). Detailed characterization of the morphology, composition, and structure of TiO_2-Ti_3C_2-F is summarized in Figs. S15, S16 and S17. NO conversion and NO_x storage selectivity for the three photocatalysts at 50 % relative humidity under UV light exposure are presented in Fig. 4a. The performance of the three photocatalysts in the oxidation of NO_x (1 ppm) is expressed in terms of $DeNO_x$ index as shown in Fig. 4b. Utilizing the $DeNO_x$ index in tandem with relative NO_x oxidation provides a better understanding of the photocatalytic performance. TiO_2 exhibits reasonable NO conversion (53 %), but produces massive amounts of NO_2 with NO_x storage selectivity of 58 % and $DeNO_x$ index of −0.10. Since NO_2 is considerably more toxic than NO, TiO_2 is clearly ineffective as a photocatalyst for NO_x removal. TiO_2-Ti_3C_2-F shows NO_x storage selectivity of 62 % and a $DeNO_x$ index of −0.05 at NO

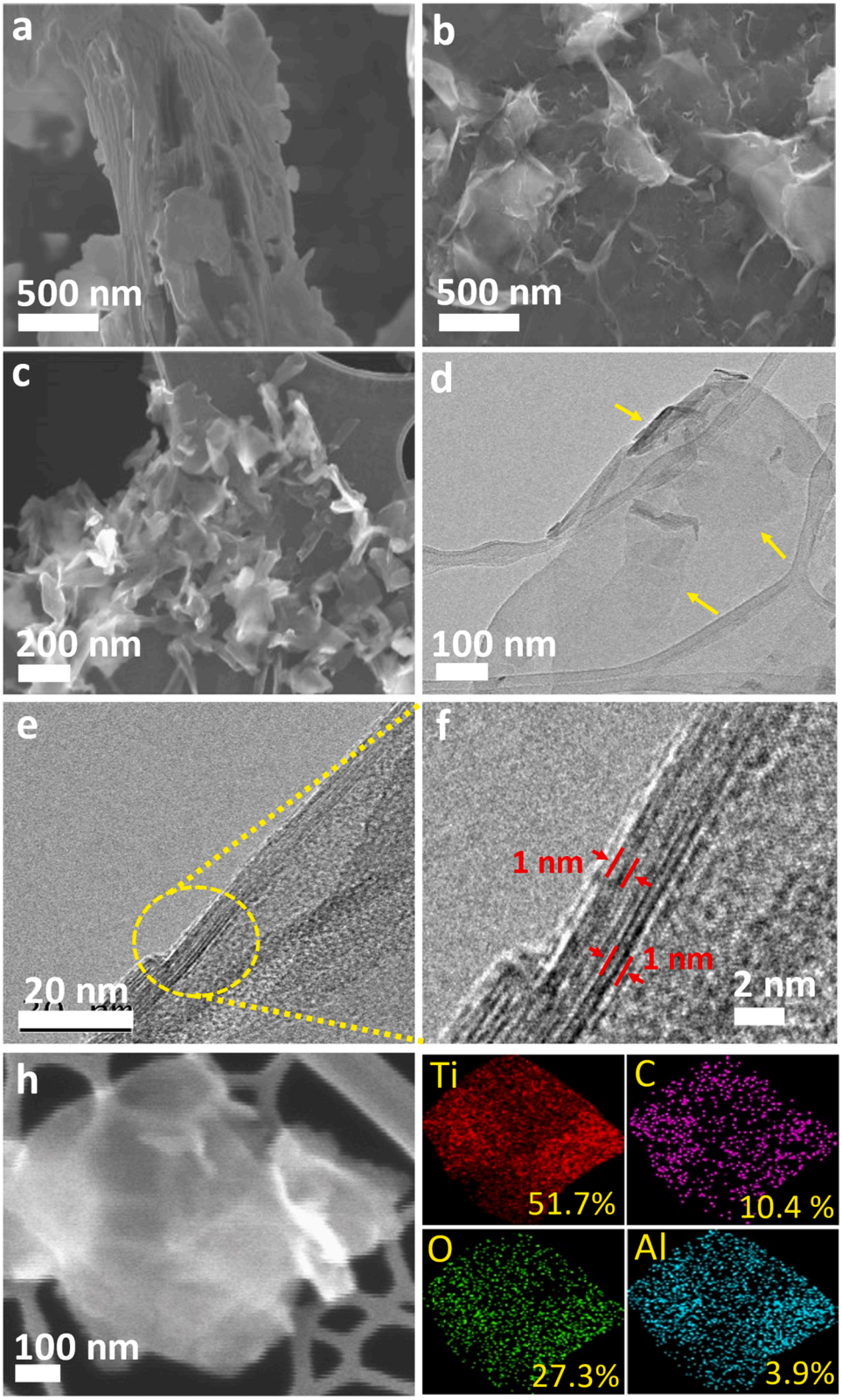

Fig. 2. SEM images of Ti_3AlC_2 (a) and E-Ti_3AlC_2 (b). (c and d) SEM and TEM images of Ti_3C_2-OH after separating the delaminated sheets via sonication and centrifugation. (e) A high-magnification TEM image of a two-layer thick Ti_3C_2-OH and (f) a zoomed-in TEM image of sheets presented in (e). (h) An SEM image of delaminated Ti_3C_2-OH and the corresponding EDS elemental mapping analysis (Ti is red, C is purple, O is green, and Al is turquoise).

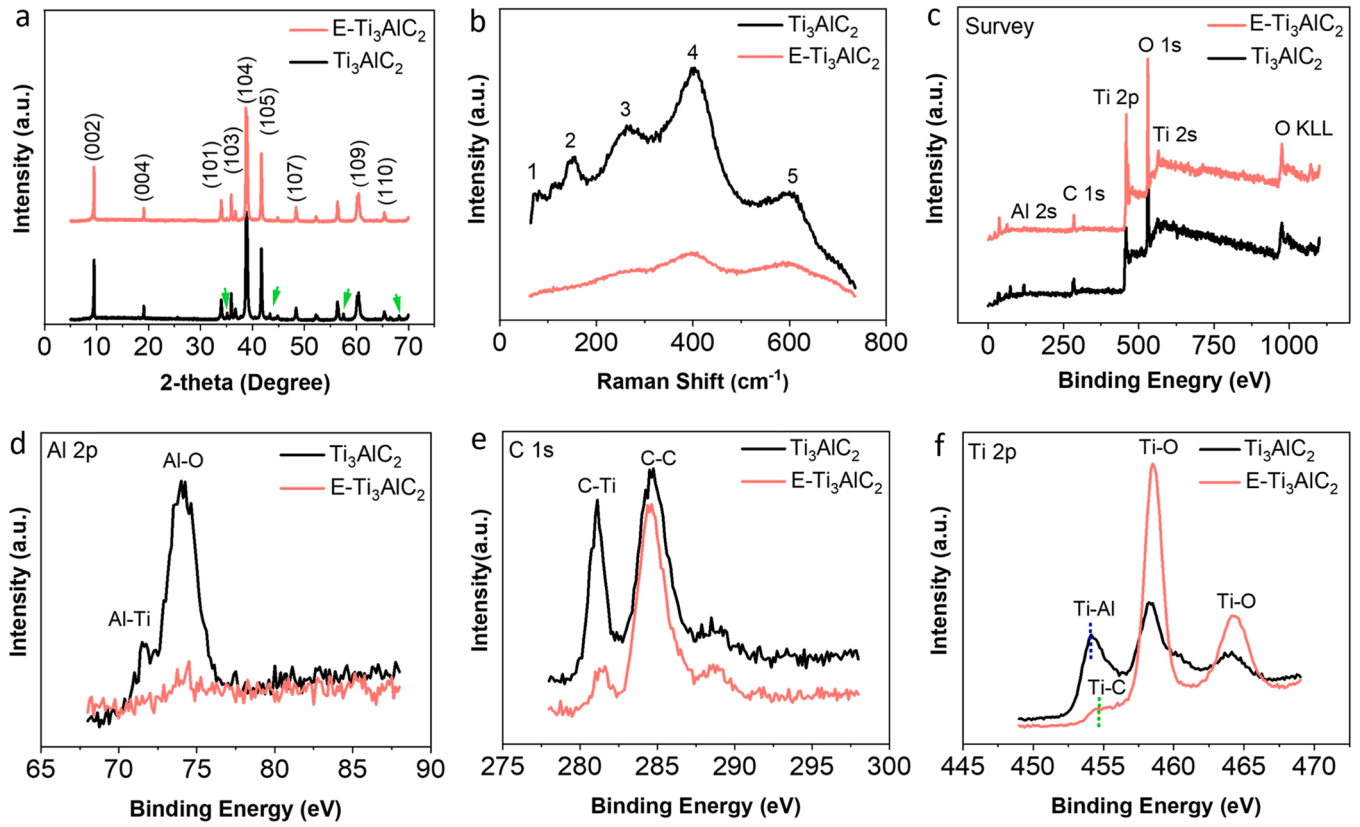

Fig. 3. Structural and chemical characterization of Ti_3AlC_2 and E-Ti_3AlC_2. (a) XRD patterns; (b) Raman spectra; (c) XPS survey scans; and high-resolution scans in Al 2p region (d), C 1 s region (e), and Ti 2p region (f).

conversion of 47 %, also indicating its ineffectiveness in photocatalytic NO_x abatement. In contrast, TiO_2-Ti_3C_2-OH exhibits outstanding performance in NO_x abatement, with excellent NO_x storage selectivity (91 %) and a positive $DeNO_x$ index of +0.30 without compromising NO conversion (54 %). When compared to other titania-based photocatalysts, tested in the same reactor and under the same conditions, TiO_2-Ti_3C_2-OH shows superior performance (Fig. 4c).

A direct comparison of the activity of TiO_2-Ti_3C_2-OH with other state-of-the-art photocatalysts in the literature can be misleading due to the different reaction conditions used. Therefore, in comparing the NO_x abatement efficiency of the photocatalysts (summarized in Table S2), the initial concentration of NO, catalyst loading, relative humidity, and emission spectrum of the light source have been considered. Reaction time is also an important factor because it affects conversion. The longer the reaction time, the lower the conversion due to photocatalyst deactivation caused by the accumulation of reaction products on the catalyst surface. Hence, for proper evaluation of the catalyst performance, we have allowed the photocatalytic reaction to run for a long period (120 min) and the averages of the data obtained are used to calculate NO conversion, selectivity and $DeNO_x$ index. The data presented in Table S2 show that our photocatalyst (TiO_2-Ti_3C_2-OH) exhibits outstanding activity in terms of selectivity and $DeNO_x$ with comparable NO conversion over the longest reaction time.

To rationalize the stark difference in photocatalytic performance of TiO_2, TiO_2-Ti_3C_2-F, and TiO_2-Ti_3C_2-OH and gain insight into the superior performance of TiO_2-Ti_3C_2-OH, it is necessary to consider the mechanism for NO_x oxidation [18,44]. The first of three steps in the photocatalytic oxidation of NO_x is the generation of charge carriers on TiO_2 surface upon light exposure (Eq. (4)). The second step is the formation of ROS via the reaction between the photogenerated charge carriers and water/oxygen molecules adsorbed on the TiO_2 surface (Eqs. (5)–(6)). The third step is the oxidation of NO adsorbed on the TiO_2 surface to NO_2 and NO_{3ads}^- (Eqs. (7)–(10)).

$$TiO_2 + hv \rightarrow TiO_2(h^+ + e^-) \quad (4)$$

$$TiO_2(h^+) + H_2O_{ads} \rightarrow TiO_2 + {}^{\cdot}OH_{ads} + H^+ \quad (5)$$

$$TiO_2(e^-) + O_{2\ ads} \rightarrow TiO_2 + O_{2\ ads}^{\cdot -} \quad (6)$$

$$NO_{ads} \xrightarrow{{}^{\cdot}OH_{ads}} HNO_{2\ ads} \xrightarrow{{}^{\cdot}OH_{ads}} NO_{2\ ads} + H_2O \quad (7)$$

$$NO_{ads} \overset{O_{2\ ads}^{\cdot -}}{\underset{H^+}{\rightarrow}} NO_{2\ ads} + {}^{\cdot}OH \quad (8)$$

$$NO_{ads} \overset{O_{2\ ads}^{\cdot -}}{\underset{H^+}{\rightarrow}} HNO_{3\ ads} \quad (9)$$

$$NO_{2\ ads} + {}^{\cdot}OH_{ads} \rightarrow HNO_{3\ ads} \rightarrow H^+ + NO_{3\ ads}^- \quad (10)$$

In addition to the generation of charge carriers upon light exposure and subsequent oxidation of NO_x by ROS, it is clear from the mechanism that the adsorption of H_2O on the catalyst surface is a significant step. The conversion rate of NO does not depend on H_2O adsorption, however, the conversion of NO_2 does. In fact, it has been shown that H_2O can displace NO_2 from the TiO_2 surface [44], a phenomenon that can prevent the interaction between the NO_2 produced and ROS, and consequently, inhibit NO_x storage selectivity. In addition, the potential dissociation of adsorbed water molecules on oxygen vacancies of TiO_2 may lead to the formation of bridging OH terminals that trap electrons and facilitate their recombination with holes, and hence reduce the concentration of ROS available for NO_x oxidation [18]. Note that reduction in ROS concentration can also occur via direct electron-hole recombination without the contribution of H_2O in TiO_2 [45]. The low amount of ROS initiates the oxidation of NO to NO_2 (Eqs. (7) and (8)), but is insufficient to store the NO_2 in the form of NO_{3ads}^- on the surface of

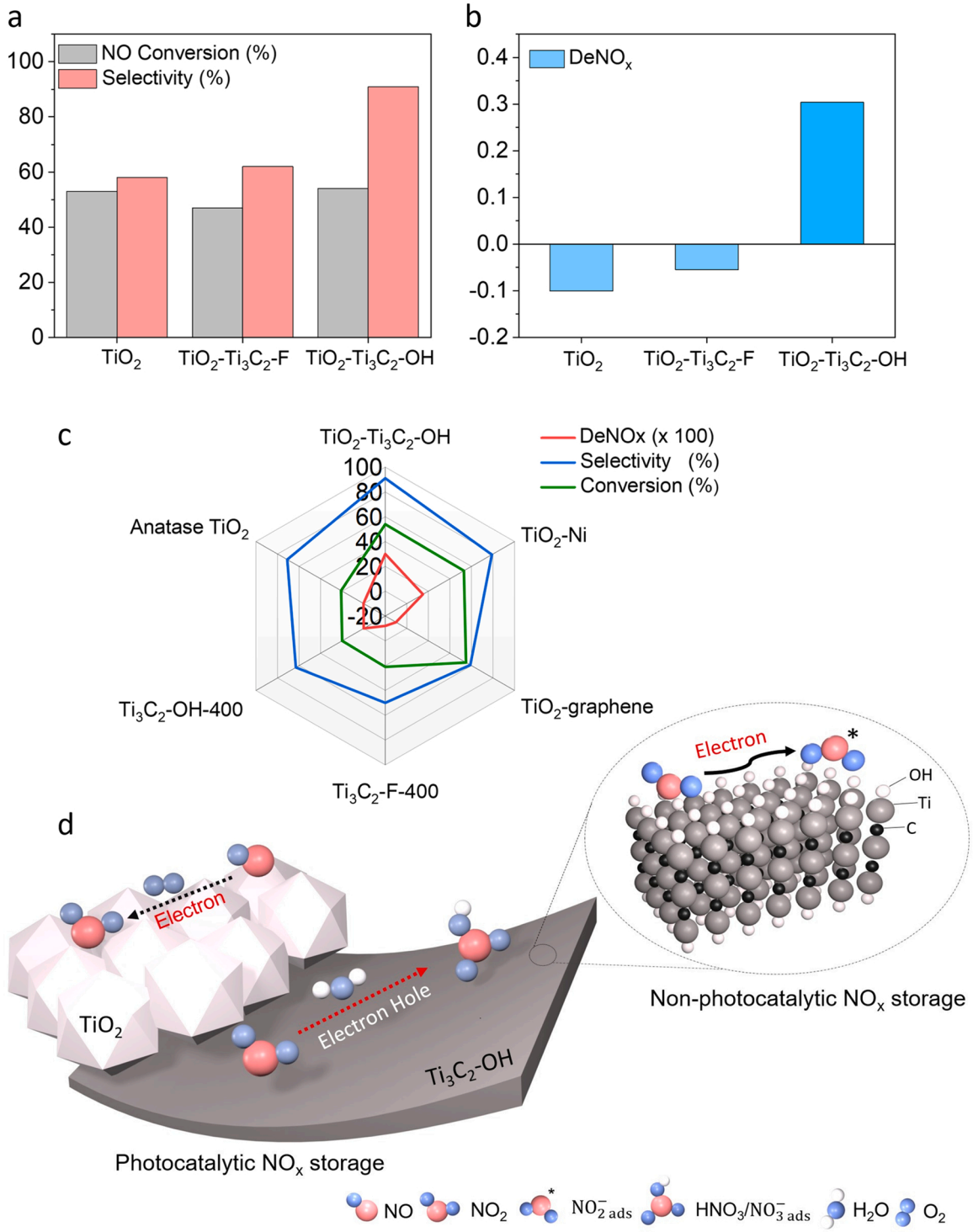

Fig. 4. (a) NO conversion and NO_x storage selectivity and (b) $DeNO_x$ index for TiO_2, TiO_2-Ti_3C_2-F, and TiO_2-Ti_3C_2-OH. (c) Spider chart comparing the performance of TiO_2-Ti_3C_2-OH with other titania-based photocatalysts. (d) Schematic illustration of NO_x abatement by TiO_2-Ti_3C_2-OH; for the sake of simplicity, the oxidation of NO to HNO_3 by photogenerated electrons and the oxidation of NO to NO_2 by photogenerated holes are not shown in the schematic.

TiO_2 (Eqs. (9) and (10)) resulting in release of NO_2 into the atmosphere. Therefore, the low $DeNO_x$ index of TiO_2 can be correlated to (1) desorption of NO_2 produced from the TiO_2 surface by adsorbed H_2O and (2) H_2O-assisted/non-H_2O-assisted charge carrier recombination.

In the case of TiO_2-Ti_3C_2-OH, NO_2 can also be displaced by H_2O from the TiO_2 surface in the same manner as described above for pristine TiO_2; however, the desorbed NO_2 adsorbs on OH terminals of Ti_3C_2 where it accepts an electron and is non-photocatalytically stored in the form of NO^-_{2ads} [8]. The same OH terminals may also act as sacrificial sites for H_2O adsorption, alleviating the competitive adsorption between NO_2 and H_2O on TiO_2, which in turn mitigates the displacement of NO_2 from TiO_2 and facilitates its subsequent oxidation. Furthermore, Ti_3C_2-OH is a known hole scavenger due to its ultralow work function [11,12,46]. Therefore, Ti_3C_2-OH in TiO_2-Ti_3C_2-OH can accept the holes and prohibits their consumption via recombination with electrons, evidenced by the observed quenching in the photoluminescence (PL)

intensity and increase in the transient photocurrent density of TiO_2 after coupling with Ti_3C_2-OH (Fig. S18a and b). Consequently, TiO_2-Ti_3C_2-OH is expected to have a higher amount of charge carriers on the surface to support the generation of more ROS for NO_x photooxidation and subsequent formation of NO^-_{3ads}. Formation of NO^-_{3ads} can also occur via the oxidation of NO^-_{2ads} that is non-photocatalytically adsorbed on Ti_3C_2-OH. In contrast to TiO_2, a high-resolution XPS scan in N 1s region of TiO_2-Ti_3C_2-OH obtained after the photocatalytic reaction (Fig. S19a) shows the presence of NO^-_{3ads} on the surface, confirming the solid-state storage of NO_x on TiO_2-Ti_3C_2-OH. The presence of NO^-_{3ads} on the surface of the used TiO_2-Ti_3C_2-OH is also confirmed by FT-IR spectroscopy (Fig. S19b). After the photocatalytic reaction, the binding energies of Ti 2p and O 1 s spectra for TiO_2-Ti_3C_2-OH show a slight shift to higher values compared to those of fresh TiO_2-Ti_3C_2-OH (Fig. S14a and b). After the reaction, however, the binding energies of Ti 2p and O1s for TiO_2-Ti_3C_2-OH are still lower than those of the fresh TiO_2. This observation suggests the accumulation of electrons on TiO_2 in the used TiO_2-Ti_3C_2-OH and that the photocatalytic process did not impact the ability of Ti_3C_2-OH to act as a hole reservoir.

Excellent NO_x abatement is therefore achieved with TiO_2-Ti_3C_2-OH due to its ability to facilitate oxidation of NO_x via photocatalytic and non-photocatalytic routes as schematically depicted in Fig. 4d. For TiO_2-Ti_3C_2-F, even though Ti_3C_2-F can reduce electron-hole recombination as shown by Ye et al. [38] and confirmed by our PL data (Fig. S20), other studies [7,8] have also shown that the presence of F terminals on the surface is unfavorable for NO_2 adsorption. Hence, it is reasonable to assume that less NO_2 molecules were adsorbed on Ti_3C_2-F in comparison to Ti_3C_2-OH, and consequently, reduced the ability of Ti_3C_2-F to store the NO_2 produced by the photocatalytic and non-photocatalytic routes, resulting in poor NO_x abatement. It is highlighted that TiO_2-Ti_3C_2-OH shows stable performance during the photocatalytic reaction, evident by the almost constant NO_2 concentration profile (Fig. S21a). However, we observed that aged TiO_2-Ti_3C_2-OH (15 days in air) exhibits lower NO_2 conversion and less stable performance compared to that of the fresh TiO_2-Ti_3C_2-OH (Fig. S21b). This observation may be attributed to the partial oxidation of Ti_3C_2-OH that gradually occurs in air, which results in the deterioration in NO_x removal performance via photocatalytic and non-photocatalytic pathways. Nevertheless, the aged TiO_2-Ti_3C_2-OH shows a higher performance than the fresh TiO_2 and fresh TiO_2-Ti_3C_2-F (Fig. S22).

4. Conclusions

In summary, we have developed a facile, fluorine-free and efficient approach to fabricate Ti_3C_2-OH. The fabrication methodology involves simultaneous etching of Al from MAX phase and intercalation with hydrazine and/or its derivative to produce thin-layered MXene. Coupling Ti_3C_2-OH with TiO_2 yields a hybrid composite (TiO_2-Ti_3C_2-OH) that exhibits outstanding NO_x abatement, evidenced by NO_x storage selectivity and $DeNO_x$ index that are superior to several other state-of-the-art titania-based photocatalysts, including hybrid photocatalysts synthesized with traditional MXene. The single-step process demonstrated in this study will not only enhance fabrication of high-quality Ti_3C_2-OH, but also reduce time and effort associated with traditional techniques that comprise two steps, especially if F-group reduction is required. In addition, this work demonstrates the pivotal role Ti_3C_2-OH plays as a co-catalyst with TiO_2 and paves a way for potential use of TiO_2-MXene hybrids in practical photocatalytic NO_x removal.

CRediT authorship contribution statement

Ahmed Al Mayyahi: Methodology, Investigation, Data curation, Formal analysis, Writing – original draft. **Swagotom Sarker:** Methodology, Conceptualization, Investigation, Writing – review & editing. **Brian Everhart:** Investigation. **Xiaoqing He:** Investigation. **Placidus Amama:** Supervision, Conceptualization, Formal analysis, Resources, Funding acquisition, Writing – review & editing.

Declaration of Competing Interest

The authors declare that they have no known competing financial interests or personal relationships that could have appeared to influence the work reported in this paper.

Acknowledgements

This study is supported by the National Science Foundation under the NSF CAREER program (Grant No. 1653527). The authors thank Professor Christopher M. Sorensen's research group for providing the graphene sample used in this study.

Appendix A. Supporting information

Supplementary data associated with this article can be found in the online version at doi:10.1016/j.mtcomm.2022.103835.

References

[1] B. Anasori, M.R. Lukatskaya, Y. Gogotsi, 2D metal carbides and nitrides (MXenes) for energy storage, Nat. Rev. Mater. 2 (2) (2017) 16098.
[2] M. Alhabeb, K. Maleski, B. Anasori, P. Lelyukh, L. Clark, S. Sin, Y. Gogotsi, Guidelines for Synthesis and Processing of Two-Dimensional Titanium Carbide (Ti3C2Tx MXene), Chem. Mater. 29 (18) (2017) 7633–7644.
[3] M. Malaki, A. Maleki, R.S. Varma, MXenes and ultrasonication, J. Mater. Chem. A 7 (18) (2019) 10843–10857.
[4] M. Seredych, C.E. Shuck, D. Pinto, M. Alhabeb, E. Precetti, G. Deysher, B. Anasori, N. Kurra, Y. Gogotsi, High-Temperature Behavior and Surface Chemistry of Carbide MXenes Studied by Thermal Analysis, Chem. Mater. 31 (9) (2019) 3324–3332.
[5] Z. Li, Y. Wu, 2D Early Transition Metal Carbides (MXenes) for Catalysis, Small 15 (29) (2019) 1804736.
[6] S.J. Kim, H.-J. Koh, C.E. Ren, O. Kwon, K. Maleski, S.-Y. Cho, B. Anasori, C.-K. Kim, Y.-K. Choi, J. Kim, Y. Gogotsi, H.-T. Jung, Metallic Ti3C2Tx MXene Gas Sensors with Ultrahigh Signal-to-Noise Ratio, ACS Nano 12 (2) (2018) 986–993.
[7] Z. Yang, A. Liu, C. Wang, F. Liu, J. He, S. Li, J. Wang, R. You, X. Yan, P. Sun, Y. Duan, G. Lu, Improvement of Gas and Humidity Sensing Properties of Organ-like MXene by Alkaline Treatment, ACS Sens. 4 (5) (2019) 1261–1269.
[8] Y. Zhang, Y. Jiang, Z. Duan, Q. Huang, Y. Wu, B. Liu, Q. Zhao, S. Wang, Z. Yuan, H. Tai, Highly sensitive and selective NO2 sensor of alkalized V2CTx MXene driven by interlayer swelling, Sens. Actuators B: Chem. 344 (2021), 130150.
[9] M. Khazaei, M. Arai, T. Sasaki, A. Ranjbar, Y. Liang, S. Yunoki, OH-terminated two-dimensional transition metal carbides and nitrides as ultralow work function materials, Phys. Rev. B 92 (7) (2015), 075411.
[10] Y. Liu, H. Xiao, W.A. Goddard, Schottky-Barrier-Free Contacts with Two-Dimensional Semiconductors by Surface-Engineered MXenes, J. Am. Chem. Soc. 138 (49) (2016) 15853–15856.
[11] X. Hu, Y. Wang, Z. Ling, H. Song, Y. Cai, Z. Li, D. Zu, C. Li, Ternary g-C3N4/TiO2/Ti3C2 MXene S-scheme heterojunction photocatalysts for NOx removal under visible light, Appl. Surf. Sci. 556 (2021), 149817.
[12] C. Peng, P. Wei, X. Li, Y. Liu, Y. Cao, H. Wang, H. Yu, F. Peng, L. Zhang, B. Zhang, K. Lv, High efficiency photocatalytic hydrogen production over ternary Cu/TiO2@Ti3C2Tx enabled by low-work-function 2D titanium carbide, Nano Energy 53 (2018) 97–107.
[13] C. Peng, X. Yang, Y. Li, H. Yu, H. Wang, F. Peng, Hybrids of Two-Dimensional Ti3C2 and TiO2 Exposing {001} Facets toward Enhanced Photocatalytic Activity, ACS Appl. Mater. Interfaces 8 (9) (2016) 6051–6060.
[14] H.S. Russell, L.B. Frederickson, O. Hertel, T. Ellermann, S.S. Jensen, A Review of Photocatalytic Materials for Urban NOx Remediation, Catalysts 11 (6) (2021) 675.
[15] B.M. Everhart, B. McAuley, A. Al Mayyahi, B. Tonyali, U. Yucel, P.B. Amama, Photocatalytic NOx Mitigation Under Relevant Conditions Using Carbon Nanotube-Modified Titania, Chem. Eng. J. (2022), 136984.
[16] J. Ma, H. Wu, Y. Liu, H. He, Photocatalytic Removal of NOx over Visible Light Responsive Oxygen-Deficient TiO2, J. Phys. Chem. C. 118 (14) (2014) 7434–7441.
[17] A. Trapalis, N. Todorova, T. Giannakopoulou, N. Boukos, T. Speliotis, D. Dimotikali, J. Yu, TiO2/graphene composite photocatalysts for NOx removal: A comparison of surfactant-stabilized graphene and reduced graphene oxide, Appl. Catal. B: Environ. 180 (2016) 637–647.
[18] M. Çağlayan, M. Irfan, K.E. Ercan, Y. Kocak, E. Ozensoy, Enhancement of photocatalytic NOx abatement on titania via additional metal oxide NOx-storage domains: Interplay between surface acidity, specific surface area, and humidity, Appl. Catal. B: Environ. 263 (2020), 118227.
[19] M. Balci Leinen, D. Dede, M.U. Khan, M. Çağlayan, Y. Koçak, H.V. Demir, E. Ozensoy, CdTe Quantum Dot-Functionalized P25 Titania Composite with Enhanced Photocatalytic NO2 Storage Selectivity under UV and Vis Irradiation, ACS Appl. Mater. Interfaces 11 (1) (2019) 865–879.

[20] Y. Li, D. Zhang, X. Feng, Y. Liao, Q. Wen, Q. Xiang, Truncated octahedral bipyramidal TiO2/MXene Ti3C2 hybrids with enhanced photocatalytic H2 production activity, Nanoscale Adv. 1 (5) (2019) 1812–1818.
[21] J.P. Wright, S. Sigdel, S. Corkill, J. Covarrubias, L. LeBan, A. Nepal, J. Li, R. Divigalpitiya, S.H. Bossmann, C.M. Sorensen, Synthesis of turbostratic nanoscale graphene via chamber detonation of oxygen/acetylene mixtures, Nano Sel. 3 (2022) 1054–1068.
[22] M.J. Friedrich, Air Pollution Is Greatest Environmental Threat to Health, JAMA 319 (11) (2018), 1085-1085.
[23] T. Li, L. Yao, Q. Liu, J. Gu, R. Luo, J. Li, X. Yan, W. Wang, P. Liu, B. Chen, W. Zhang, W. Abbas, R. Naz, D. Zhang, Fluorine-Free Synthesis of High-Purity Ti3C2Tx (T=OH, O) via Alkali Treatment, Angew. Chem. Int. Ed. 57 (21) (2018) 6115–6119.
[24] X. Xie, Y. Xue, L. Li, S. Chen, Y. Nie, W. Ding, Z. Wei, Surface Al leached Ti3AlC2 as a substitute for carbon for use as a catalyst support in a harsh corrosive electrochemical system, Nanoscale 6 (19) (2014) 11035–11040.
[25] H.W. Lucien, Thermal Decomposition of Hydrazine, J. Chem. Eng. Data 6 (4) (1961) 584–586.
[26] Q. Zhang, J. He, X. Fu, S. Xie, R. Fan, H. Lai, W. Cheng, P. Ji, J. Sheng, Q. Liao, W. Zhu, H. Li, Fluorine-free strategy for hydroxylated Ti3C2/Ti3AlC2 catalysts with enhanced aerobic oxidative desulfurization and mechanism, Chem. Eng. J. 430 (2022), 132950.
[27] A. Sengupta, B.V.B. Rao, N. Sharma, S. Parmar, V. Chavan, S.K. Singh, S. Kale, S. Ogale, Comparative evaluation of MAX, MXene, NanoMAX, and NanoMAX-derived-MXene for microwave absorption and Li ion battery anode applications, Nanoscale 12 (15) (2020) 8466–8476.
[28] M. Naguib, M. Kurtoglu, V. Presser, J. Lu, J. Niu, M. Heon, L. Hultman, Y. Gogotsi, M.W. Barsoum, Two-Dimensional Nanocrystals Produced by Exfoliation of Ti3AlC2, Adv. Mater. 23 (37) (2011) 4248–4253.
[29] T.B. Limbu, B. Chitara, M.Y. Garcia Cervantes, Y. Zhou, S. Huang, Y. Tang, F. Yan, Unravelling the Thickness Dependence and Mechanism of Surface-Enhanced Raman Scattering on Ti3C2TX MXene Nanosheets, J. Phys. Chem. C. 124 (32) (2020) 17772–17782.
[30] A. Sarycheva, Y. Gogotsi, Raman Spectroscopy Analysis of the Structure and Surface Chemistry of Ti3C2Tx MXene, Chem. Mater. 32 (8) (2020) 3480–3488.
[31] A.C. Ferrari, Raman spectroscopy of graphene and graphite: Disorder, electron–phonon coupling, doping and nonadiabatic effects, Solid State Commun. 143 (1) (2007) 47–57.
[32] A.C. Ferrari, J. Robertson, A.C. Ferrari, J. Robertson, Raman spectroscopy of amorphous, nanostructured, diamond–like carbon, and nanodiamond, Philos. Trans. R. Soc. Lond. Ser. A: Math., Phys. Eng. Sci. 2004 (362) (1824) 2477–2512.
[33] L.-Å. Näslund, P.O.Å. Persson, J. Rosen, X-ray Photoelectron Spectroscopy of Ti3AlC2, Ti3C2Tz, and TiC Provides Evidence for the Electrostatic Interaction between Laminated Layers in MAX-Phase Materials, J. Phys. Chem. C. 124 (50) (2020) 27732–27742.
[34] R.B. Rakhi, B. Ahmed, M.N. Hedhili, D.H. Anjum, H.N. Alshareef, Effect of Postetch Annealing Gas Composition on the Structural and Electrochemical Properties of Ti2CTx MXene Electrodes for Supercapacitor Applications, Chem. Mater. 27 (15) (2015) 5314–5323.
[35] V. Natu, M. Benchakar, C. Canaff, A. Habrioux, S. Célérier, M.W. Barsoum, A critical analysis of the X-ray photoelectron spectra of Ti3C2Tz MXenes, Matter 4 (4) (2021) 1224–1251.
[36] G. Li, L. Tan, Y. Zhang, B. Wu, L. Li, , Highly Efficiently Delaminated Single-Layered MXene Nanosheets with Large Lateral Size, Langmuir 33 (36) (2017) 9000–9006.
[37] F. Han, S. Luo, L. Xie, J. Zhu, W. Wei, X. Chen, F. Liu, W. Chen, J. Zhao, L. Dong, K. Yu, X. Zeng, F. Rao, L. Wang, Y. Huang, Boosting the Yield of MXene 2D Sheets via a Facile Hydrothermal-Assisted Intercalation, ACS Appl. Mater. Interfaces 11 (8) (2019) 8443–8452.
[38] M. Ye, X. Wang, E. Liu, J. Ye, D. Wang, Boosting the Photocatalytic Activity of P25 for Carbon Dioxide Reduction by using a Surface-Alkalinized Titanium Carbide MXene as Cocatalyst, ChemSusChem 11 (10) (2018) 1606–1611.
[39] Y. Liao, J. Qian, G. Xie, Q. Han, W. Dang, Y. Wang, L. Lv, S. Zhao, L. Luo, W. Zhang, H.-Y. Jiang, J. Tang, 2D-layered Ti3C2 MXenes for promoted synthesis of NH3 on P25 photocatalysts, Appl. Catal. B: Environ. 273 (2020), 119054.
[40] S. Debow, T. Zhang, X. Liu, F. Song, Y. Qian, J. Han, K. Maleski, Z.B. Zander, W. R. Creasy, D.L. Kuhn, Y. Gogotsi, B.G. DeLacy, Y. Rao, Charge Dynamics in TiO2/MXene Composites, J. Phys. Chem. C. 125 (19) (2021) 10473–10482.
[41] Z. Lu, L. Zeng, W. Song, Z. Qin, D. Zeng, C. Xie, In situ synthesis of C-TiO2/g-C3N4 heterojunction nanocomposite as highly visible light active photocatalyst originated from effective interfacial charge transfer, Appl. Catal. B: Environ. 202 (2017) 489–499.
[42] Z. Zhang, J.T. Yates, Band Bending in Semiconductors: Chemical and Physical Consequences at Surfaces and Interfaces, Chem. Rev. 112 (10) (2012) 5520–5551.
[43] F. Xu, K. Meng, B. Cheng, S. Wang, J. Xu, J. Yu, Unique S-scheme heterojunctions in self-assembled TiO2/CsPbBr3 hybrids for CO_2 photoreduction, Nat. Commun. 11 (1) (2020) 4613.
[44] L. Yang, A. Hakki, F. Wang, D.E. Macphee, Different Roles of Water in Photocatalytic DeNOx Mechanisms on TiO2: Basis for Engineering Nitrate Selectivity? ACS Appl. Mater. Interfaces 9 (20) (2017) 17034–17041.
[45] A. Al Mayyahi, B.M. Everhart, T.B. Shrestha, T.C. Back, P.B. Amama, Enhanced charge separation in TiO2/nanocarbon hybrid photocatalysts through coupling with short carbon nanotubes, RSC Adv. 11 (19) (2021) 11702–11713.
[46] X.-H. Zha, Q. Huang, J. He, H. He, J. Zhai, J.S. Francisco, S. Du, The thermal and electrical properties of the promising semiconductor MXene Hf2CO2, Sci. Rep. 6 (1) (2016) 27971.